

**Impact of oxygen on the 300-K isotherm of Laser Megajoule ablator using *ab initio* simulation**P. Colin-Lalu,<sup>1,2,\*</sup> V. Recoules,<sup>1</sup> G. Salin,<sup>1</sup> and G. Huser<sup>1</sup><sup>1</sup>CEA, DAM/DIF, Bruyères-le-Château, F-91297 Arpajon, France<sup>2</sup>Laboratoire pour l'Utilisation des Lasers Intenses (LULI), École Polytechnique, F-91128 Palaiseau, France

(Received 8 June 2015; revised manuscript received 11 September 2015; published 9 November 2015)

The ablator material for inertial confinement fusion (ICF) capsules on the Laser Mégajoule is a glow-discharge polymer (GDP) plastic. Its equation of state (EOS) is of primary importance for the design of such capsules, since it has direct consequences on shock timing and is essential to mitigate hydrodynamic instabilities. Using *ab initio* molecular dynamics (AIMD), we have investigated the 300-K isotherm of amorphous  $\text{CH}_{1.37}\text{O}_{0.08}$  plastic, whose structure is close to GDP plastic. The 300-K isotherm, which is often used as a cold curve within tabular EOS, is an important contribution of the EOS in the multimegabar pressure range. AIMD results are compared to analytic models within tabular EOS, pointing out large discrepancies. In addition, we show that the effect of oxygen decreases 300-K isotherm pressure by 10%–15%. The implication of these observations is the ability to improve ICF target performance, which is essential to achieve fusion ignition.

DOI: [10.1103/PhysRevE.92.053104](https://doi.org/10.1103/PhysRevE.92.053104)

PACS number(s): 52.57.Bc, 64.30.–t

**I. INTRODUCTION**

Inertial confinement fusion (ICF) requires using large scale laser facilities to implode and ignite a spherical capsule made of an ablator layer surrounding a cryogenic deuterium-tritium (D-T) mixture [1]. During the implosion of the capsule, the density and temperature have to increase enough to trigger thermonuclear reactions at the center of the capsule. This requires a stable implosion arising from a high implosion velocity, favored by a low solid density of the ablator material. Light materials such as Be, high density carbon, and plastic (CH) [2] are thus particularly suitable as ablator materials. Among all these materials, the CH ablator has been the subject of numerous experimental [3,4] and theoretical [5–10] studies, and is the chosen material for ICF capsules on the Laser Megajoule.

The equation of state (EOS) of such ablator materials plays a central role in achieving fusion ignition. First, it is a key parameter in mitigating hydrodynamic instabilities occurring during the implosion process [11]. Second, precise knowledge of the ablator EOS is required to determine shock timing [12], which has to be fine tuned down to a precision of 50 ps [13]. Up to now, EOS models such as the quotidian equation of state (QEOS) [14] and SESAME [15] have been used to generate wide-ranging EOS tables. These combine several analytic models in order to produce a tabular EOS to be used in hydrodynamic simulation codes. However, analytic modeling is insufficient in the warm, dense matter regime to construct a precise EOS, given that quantum effects are important [14]. Recent EOS studies include both *ab initio* molecular dynamics (AIMD) simulations [16] and experiments to constrain EOS models. AIMD associates the density functional theory (DFT) to classical molecular dynamics, which is particularly suitable to simulate warm, dense systems. In parallel, laser-shock wave experiments constrain AIMD and model predictions through high precision Hugoniot measurements [3,4].

Among the parameters that can be improved within EOS tables, the cold curve is an important contribution in the

multimegabar pressure range, since pressure on the Hugoniot is written as the sum of pressures arising from the cold curve and the thermal effects of ions and electrons. For example, using the QEOS model for polystyrene, the cold curve contribution ranges from 55% of shock pressure at 1 Mbar, to 25% at 10 Mbar, and 15% at 20 Mbar. Knowing the cold curve is thus essential to determine precisely the thermodynamic path of the capsule. Generally, the cold curve is constructed at zero temperature by adapting plasma EOS models [14] or by extrapolating high-temperature AIMD predictions [9] and/or experimental Hugoniot measurements.

Another issue that has recently been addressed is the chemical composition of the plastic ablator material used in ICF capsules [17,18]. Until recently, most of the CH ablator EOS studies have been performed on polystyrene. However, the plastic used in the ablator layer of ICF targets is a glow-discharge polymer (GDP) whose structure is determined by the fabrication process. GDP plastic has an amorphous structure and contains a small fraction of oxygen, in addition to carbon and hydrogen (unlike polystyrene). Recent works have shown the importance of taking into account the oxygen within the plastic ablator shells. It affects the shock velocity during ICF capsule implosion by absorbing x rays [17] and increases hydrodynamic instabilities by a factor 3–5 times larger than contributions from the surface roughness [18]. The EOS of the ablator material in plastic is changed by the presence of oxygen, in particular, the cold curve, since it is highly dependent on the atomic structure of solid matter.

Recent AIMD studies on CH ablators produced EOS data along isochores [5,6], principal Hugoniot [7,8], as well as overextended  $(\rho, T)$  regions of the phase diagram [9,10]. These studies deal with the liquid states of idealized CH materials. Here, we investigate a solid structure of amorphous  $\text{CH}_{1.37}\text{O}_{0.08}$ , which is a representation of GDP plastic. The 300-K isotherm is constructed with up to ten times compression using AIMD simulations. This 300-K isotherm can be assimilated to the cold curve used in EOS tables for ICF applications. Moreover, our results will be compared to diamond anvil cell experiments, which will be presented in a forthcoming paper. The effect of the presence of oxygen along this isotherm is studied in order to improve the tabular

\*[pierre.colin-lalu@polytechnique.edu](mailto:pierre.colin-lalu@polytechnique.edu)

EOS used to design ICF experiments. GDP characterization is detailed in Sec. II. AIMD calculations are described in Sec. III. Results are then compared to current models within tabular EOS in Sec. IV. We conclude by discussing the implications for ICF.

## II. GLOW-DISCHARGE POLYMER PLASTIC CHARACTERISTICS

Investigating the 300-K isotherm involves knowing the atomic structure of matter. The GDP ablator layer of ICF capsules is a plastic composed of hydrogenated amorphous carbon. This amorphous property is due to the plasma enhanced chemical vapor deposition coating method [19]. Low energetic species (1–5 eV) are deposited on a substrate by dissociating a trans-2-butene gas ( $C_2H_8$ ) with a hydrogen gas ( $H_2$ ) in an inductively coupled plasma generated using high frequency discharge (46 MHz). Upon dissociation of  $C_2H_8$  and reaction with  $H_2$ , atoms make bonds between them and form an amorphous polymer. The average atomic composition of each element is 40% of carbon and 60% of hydrogen just after the glow-discharge polymerization process. X-ray diffraction measurements of a GDP sample in a diamond anvil cell [20] have confirmed its amorphous property and a lack of crystallization up to 20 GPa.

Upon storage, oxygen enters the chemical composition of GDP plastic. A recent study has shown that GDP plastic contains unsaturated bonds on which oxygen and hydrogen atoms are irreversibly absorbed within the first 20–50  $\mu\text{m}$  [17].

The atomic composition of GDP plastic has been investigated by the CEA/Valduc target group by using Rutherford backscattering spectroscopy (RBS) on 300 nm thick samples [21]. These measurements were then confirmed by infrared (IR) spectroscopy measurements under nitrogen pyrolysis at 1080 °C of 5  $\mu\text{m}$  thick samples. Results showed that the atomic proportion of oxygen increases up to 3% after several months of storage, in good agreement with measurements performed by Huang *et al.* [17]. The atomic composition of GDP plastic used in AIMD simulations is 41% carbon, 56% hydrogen, and 3% oxygen. The solid density of GDP plastic has also been measured to be  $1.07 \pm 0.03 \text{ g/cm}^3$  and the sound speed was measured to be  $2667 \pm 28 \text{ m/s}$  using Brillouin oscillations [22].

## III. AB INITIO MOLECULAR DYNAMICS SIMULATIONS

Simulations are performed using the *ab initio* molecular dynamics (AIMD) approach implemented in the ABINIT package [23–25]. Based upon the Born-Oppenheimer approximation, the electrons adjust to the spatial arrangement of ions. AIMD associates a quantum treatment for electrons using the density functional theory (DFT) to classical molecular dynamics for ions.

The projector augmented wave (PAW) method [26,27] is used for the electronic plane-wave implementation of the DFT [28]. We use PAW potentials for H, C, and O (with valence orbitals of  $1s^1$ ,  $2s^22p^2$ , and  $2s^22p^4$ , respectively, and core radii of 1, 1.1, and 1.2 a.u.) [5].  $\Gamma$ -point sampling of the first Brillouin zone is used for AIMD simulations. The cutoff energy for the plane-wave basis is equal to 30 Ha

TABLE I. Number of atoms of each element in a simulation cell of 250 atoms.

Configuration	C	H	O
CH	100	150	
CHO	102	140	8

(816.34 eV). The exchange-correlation energy is determined by the generalized gradient approximation (GGA) according to the parametrization of Perdew, Burke, and Ernzerhof [29].

The isokinetic ensemble is used for the molecular dynamics with cubic simulation cells containing 250 atoms. This *NVT* ensemble keeps the temperature constant by rescaling the velocities at each time step, and the equation of motion of ions is solved by the algorithm proposed by Minary *et al.* [30,31]. The dynamics of the atoms is simulated to within a few picoseconds.

Our current knowledge of GDP plastic is limited to its amorphous nature and to its chemical composition (described in Sec. II.). We therefore choose to generate an amorphous structure using a melt-and-quench method in order to represent GDP plastic in standard conditions. This structure is then compressed at 300 K in order to generate an isotherm. The effect of oxygen upon the 300-K isotherm is studied by the use of two different atomic configurations, so called CH (C: 40%, H: 60%) and CHO (C: 41%, H: 56%, O: 3%).

Two structures are generated at  $1.07 \text{ g/cm}^3$  for the CH and CHO configurations. A melt is performed at high temperature (3000 K), followed by a quick quench to freeze an atomic structure at 300 K with temperature thresholds at 2000 and 1000 K. At each temperature threshold, dynamics simulation is simulated within 2 ps with a time step of 0.25 fs in the *NVT* ensemble. The equilibrium is then checked by running simulations in an *NVE* ensemble for 1 ps. Once equilibrium is reached at 3000 K, the temperature is then forcefully lowered to 2000 K and then to 1000 K. These temperature thresholds are used to get stable random atomic positions in the simulation cell. Bonds are formed during the last step of the relaxation of the system between 1000 and 300 K.

Each structure uses the atomic composition defined in Table I. An analysis of the partial radial distribution functions (RDFs) between ions (Fig. 1) shows that the distance of the first peak for the C–H bond and the H–H bond, as well as the coordination numbers, do not change between both structures. They are respectively around 1.12 Å for the C–H bond and around 0.78 Å for the H–H bond. However, the presence of oxygen in the CHO structure modifies the nature of the C–C bonding. For CH, RDF displays two peaks, whose locations correspond to a single C–C bond type (1.53 Å) and a double C=C bond type (1.34 Å), according to the chemical handbook data [32]. The CHO structure (containing oxygen) displays an extra triple C≡C bond type at 1.23 Å. This atomic arrangement suggests that the compression property of the carbon-carbon skeleton is modified with the insertion of oxygen atoms. Consequently, the 300-K isotherms for both structures will have different slopes. Due to the small number of oxygen atoms (eight atoms) inside our simulation cell, the analysis of partial distribution functions between the oxygen and other species is not relevant.

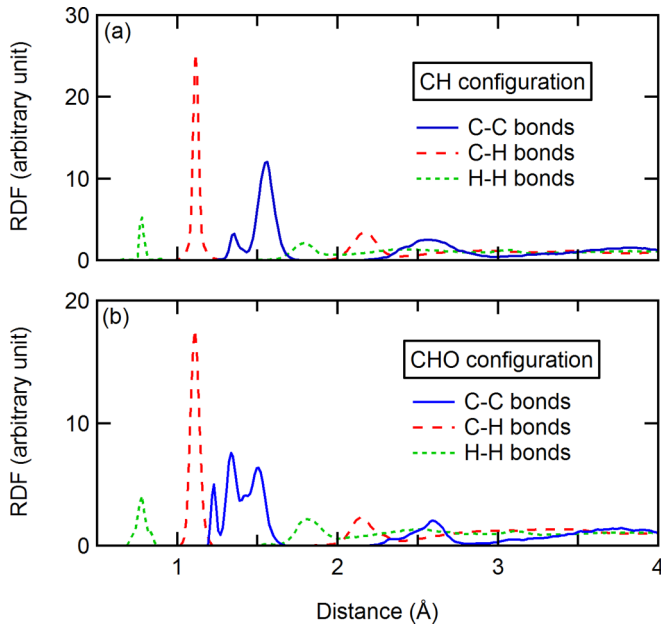


FIG. 1. (Color online) AIMD calculated radial pair correlation functions of (a) CH and (b) CHO configurations at ambient temperature (300 K) and at density ( $\rho_0 = 1.07 \text{ g/cm}^3$ ).

The 300-K isotherm of CHO plastic is then constructed by compressing the atomic structure previously quenched at  $1.07 \text{ g/cm}^3$  and 300 K. This method uses as a starting point the reduced coordinates of atoms. The density is determined by cell resizing and remains constant during the simulation, as well as temperature (set at 300 K). The molecular dynamics runs for a few picoseconds. Equilibrium is reached after 500 fs of simulation. The pressure is then averaged along the equilibrium trajectory during the last 500 fs. The amplitude of the statistical fluctuations is around 10% at low pressure and below 1% for pressures higher than 100 GPa. We checked that the simulation boxes are homogeneous and contain no voids. In order to check that simulated states are independent of the starting point, other simulations are performed using reduced atomic coordinates equilibrated along the isotherm. These give pressures that are reproducible to within 0.4%. The simulation results are given in Table II.

Figure 2 displays the AIMD data points for CHO in a low density range. The error bars are due to pressure fluctuations in the AIMD simulations and pressure reproducibility. Pressure-density concavity reverses at around  $1.8$  and around  $2.2 \text{ g/cm}^3$ . By looking at RDF for the C–C bond, these concavity changes correspond to the vanishings of the first peak at  $1.23 \text{ \AA}$  around  $1.8 \text{ g/cm}^3$ , followed by the second peak at  $1.34 \text{ \AA}$  around  $2.2 \text{ g/cm}^3$  (Fig. 1). The carbon bonds are broken when the atomic structure is compressed, leading to local increases of compressibility. The atomic structures for density above  $2.2 \text{ g/cm}^3$  keep one peak for the C–C bond at around  $1.53 \text{ \AA}$ . These AIMD predictions need to be confirmed by static pressure-density experimental measurements, such as diamond anvil cell experiments.

The 300-K isotherm of CH is constructed using the same method (see the simulation results in Table III). Note that below  $1.8 \text{ g/cm}^3$ , pressures for the CH and CHO configurations are

TABLE II. AIMD data points calculated for the CHO configuration (41 at. % carbon, 56 at. % hydrogen, 3 at. % oxygen).

$\rho \text{ (g/cm}^3\text{)}$	$P \text{ (GPa)}$	$\Delta P \text{ (GPa)}$
1.07	2.72	0.39
1.177	4.23	0.46
1.284	6.36	0.46
1.391	9.35	0.5
1.498	12.79	0.67
1.605	16.97	0.64
1.712	22.5	0.69
1.819	25.68	0.79
1.926	31.26	0.71
2.033	39.16	0.71
2.14	47.83	0.95
2.247	54.05	0.78
2.461	77.5	1.2
2.675	105.1	1.2
3.21	193.38	1.7
3.745	314.52	2.3
4.28	471.32	3
4.815	652.58	3.8
5.35	864.22	4.7
6.42	1373	6.9
7.49	2010	9.5
8.56	2777	13
9.63	3677	17
10.7	4695	21

the same within 2–3 GPa. For higher densities, pressures for the structure with oxygen are lower than the structure without oxygen. A significant pressure difference is observed along the isotherm (Fig. 3). These are about 9 GPa at  $2.14 \text{ g/cm}^3$ , about 102 GPa at  $5.35 \text{ g/cm}^3$ , and about 465 GPa at  $10.7 \text{ g/cm}^3$ .

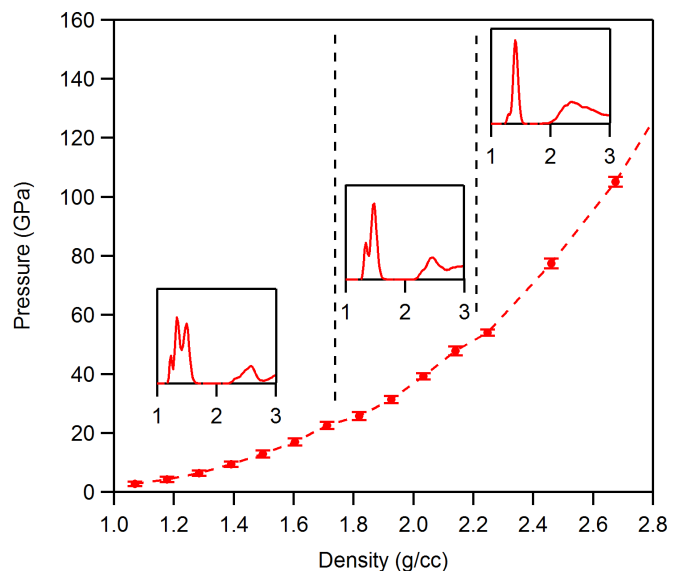


FIG. 2. (Color online) AIMD data points for GDP-CHO. Pressures in red arise from a compression of the atomic structure quenched at  $1.07 \text{ g/cm}^3$ . The insets display the RDFs of the C–C bonds.

TABLE III. AIMD data points calculated for the CH configuration (40 at. % carbon, 60 at. % hydrogen).

$\rho$ (g/cm <sup>3</sup> )	$P$ (GPa)	$\Delta P$ (GPa)
1.07	0.85	0.25
1.284	4.31	0.33
1.391	7.21	0.46
1.498	11.46	0.62
1.605	16.38	0.73
2.14	56.28	0.97
3.21	232.95	1.9
4.28	540.54	3.5
5.35	966.28	5.1
6.42	1540	7.6
7.49	2238	11
8.56	3088	14
9.63	4059	18
10.7	5160	22

#### IV. MODELING OF COLD CURVE

We now focus on the CHO structure, which is the most relevant representation of GDP plastic used as an ICF capsule ablator material. The AIMD 300-K isotherm is compared with parametric EOS as well as analytic models commonly used to construct the cold curve in tabular EOS.

##### A. Parametric EOS forms

Several EOS forms have been developed to parametrize the zero-temperature isotherm. These give pressure as a function of density using solid density  $\rho_0$ , bulk modulus  $K_0$ , and its derivatives as parameters.

The most common parametric EOS forms use either the theory of finite strain, or an effective potential [33]. The third-order Birch-Murnaghan (BM3) form is based on the former and uses a series expansion of the strain energy in terms of

Eulerian strain [34]. Isochore pressures are calculated as

$$P_c^{\text{BM3}}(x) = 1.5K_0(x^{-7} - x^{-5})[1 + 0.75(K'_0 - 4)(x^{-2} - 1)],$$

where  $x = (\rho_0/\rho)^{1/3}$  for convenience.

Other parametric EOS consider nearest neighbor interactions of an idealized solid at zero temperature to determine an interatomic potential. The first form we use was proposed by Vinet [35], resulting from an effective Rydberg potential. It gives the following pressure-density relation:

$$P_c^{\text{Vinet}}(x) = 3K_0 \frac{1-x}{x^2} \exp\left\{\frac{3}{2}(K'_0 - 1)(1-x)\right\}.$$

This form was then modified by Holzapfel [36] in order to correct the strong asymptotic behavior at high compression. An adapted second-order polynomial expansion (AP2) was added, providing the correct Thomas-Fermi limit at infinite compression. Within this parametrization, the pressure is given as

$$P_c^{\text{AP2}}(x) = 3K_0 \frac{1-x}{x^5} \exp\{c_0(1-x)\}[1 + c_2x(1-x)],$$

with  $c_2 = 3/2(K'_0 - 3) - c_0$ , and  $c_0 = -\ln(3K_0/p_{\text{FG0}})$ , where  $p_{\text{FG0}}$  is the effective Fermi gas pressure  $p_{\text{FG0}} = a_{\text{FG}}(Z/V_0)^{5/3}$ , which contains the Fermi gas parameter  $a_{\text{FG}} = 23.37 \text{ MPa nm}^5$ .

We have used these parametric EOS forms to fit AIMD data points in the 2.24–10.7 g/cm<sup>3</sup> density range only, since these do not take into account changes in the microscopic structures. These fits were constrained with values experimentally measured for parameters  $\rho_0$  and  $K_0$ . They are  $\rho_0 = 1.07 \text{ g/cm}^3$  and  $K_0 = c_0^2 \rho_0 = 7.6108 \text{ GPa}$ .

Figure 4 displays the difference in pressure between these fits and the AIMD data points. BM3 EOS fails at fitting the AIMD data points using physical parameters for  $\rho_0$  and  $K_0$ . The Vinet EOS gets better results with  $K'_0 = 6.488$ . The differences between AIMD and fitted pressures show a maximum deviation of 23 GPa. The AP2 EOS provides the lowest discrepancies in a domain of pressure up to 4500 GPa

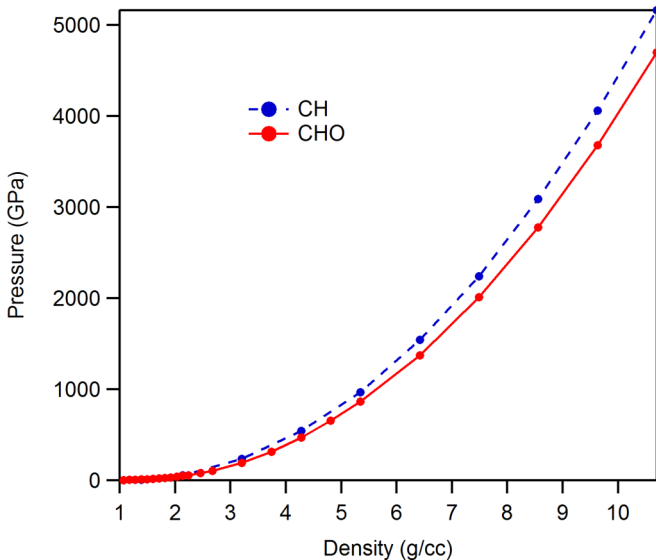


FIG. 3. (Color online) AIMD data points for CH (in blue) and CHO (in red) configurations.

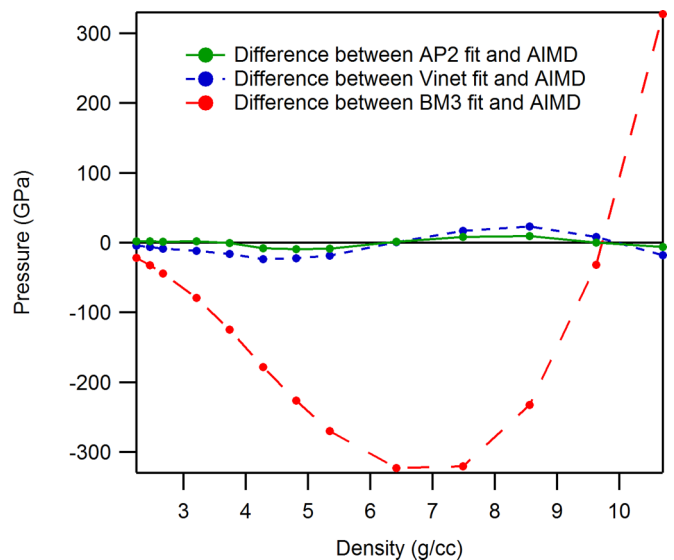


FIG. 4. (Color online) Pressure difference between parametric EOS models and AIMD data points for CHO.

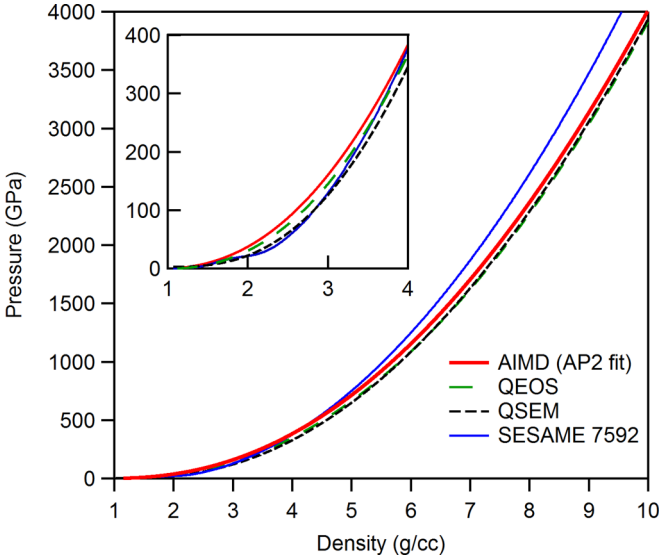


FIG. 5. (Color online) AP2 fit to AIMD calculations compared to tabular EOS. The red curve shows parametric AP2 fits to calculations (see Sec. IV) for the CHO configuration. The cold curve given by SESAME 7592 is displayed by the dashed blue curve. The green and gray curves come from the QEOS and the QSEM for CHO. The inset shows details in the 1–4 g/cm<sup>3</sup> density range.

with a maximum deviation of 9 GPa (Fig. 4). We choose the AP2 fit to represent AIMD data thereafter with the following parameters:  $\rho_0 = 1.07$ ,  $K_0 = 7.6108$ ,  $K'_0 = 8.3204$ ,  $c_0 = 2.2948$ .

### B. Comparison with models used in tabular EOS

We now compare AIMD predictions to cold curves extracted from two analytic EOS models that we use to construct tabular EOS: QEOS [14] and quantum semiempirical model (QSEM) [37].

Both EOSs use theoretical models to calculate ionic and electronic contributions of each element separately. These models are entirely analytic and can be scaled using only the atomic number  $Z$  and atomic mass  $A$  of each element. The EOS for the CHO configuration, which is a mixture of carbon, hydrogen, and oxygen atoms, is then calculated using an isobaric-isothermal mixing rule for electrons and an average atom model for ions.

Using QEOS, the thermodynamics of atoms is described by the use of the Cowan model and electrons by the Thomas-Fermi semiclassical model. Thomas-Fermi theory gives a positive pressure produced by the gas of free electrons at zero temperature. A semiempirical bonding correction developed by Barnes [38] is then applied to obtain an approximately correct equation of state in the low density range. It calculates a pressure correction  $P_{\text{corr}}$  so that the pressure of the mixture  $P_c(\rho) = P_{\text{ions}}(\rho) + P_{\text{electrons}}(\rho) + P_{\text{corr}}$  retrieves normal conditions for the bulk properties described by the condition

$$P_c(\rho_0, T_0) = P_0,$$

$$\rho \frac{\partial P_c}{\partial \rho}(\rho_0, T_0) = K_0.$$

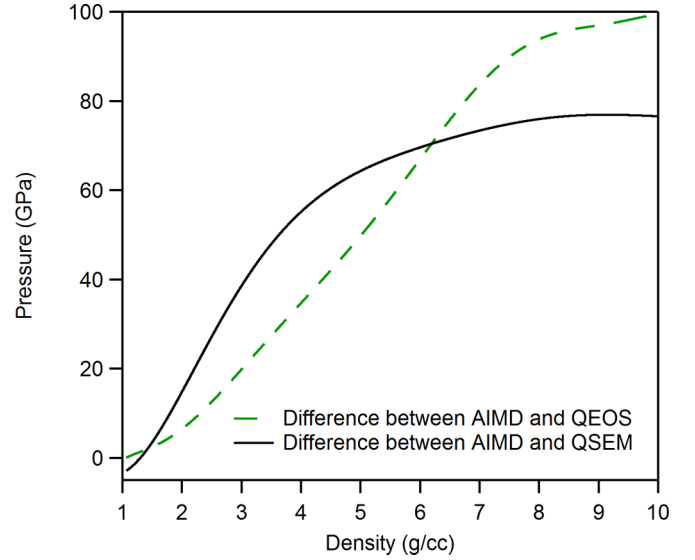


FIG. 6. (Color online) Pressure difference between the parametric AP2 fit to AIMD data points (see Sec. IV) and models used in tabular EOS for the CHO configuration.

This correction is performed with  $\rho_0 = 1.07$  g/cm<sup>3</sup> and  $K_0 = 7.6108$  GPa at  $T_0 = 300$  K and  $P_0 = 1$  bar.

In QSEM, the thermodynamics of atoms is still described by the use of the Cowan model. However, a quantum treatment of electrons is employed by the use of the Inferno option [39] of the variational average atom in quantum plasmas (VAAQP) code [40]. Pressure is directly given by the code without applying a semiempirical correction. Both curves in the 1–10 times  $\rho_0$  density range use a Debye solid model for the ionic part, implemented in the Cowan model.

Figure 5 displays the analytical models for CHO and AP2 fit to the AIMD data points. The models used in tabular EOS produce pressures lower than the *ab initio* molecular dynamics. The pressure discrepancy increases along the density (Fig. 6). It stabilizes around 70 GPa at 5 g/cm<sup>3</sup> for QSEM. The QEOS model gives pressures close to the AIMD data points at low density. The difference increases slowly to stabilize around 95 GPa at 8 g/cm<sup>3</sup>, which corresponds to less than 4%. The pressure-density concavity is similar between cold curves after these density thresholds. However, the curvature discrepancy is large at low density, which will change the principal Hugoniot curvature.

### V. CONCLUSION

Using AIMD, we have constructed the 300-K isotherm of glow-discharge polymer plastic used in ICF capsules for Laser Megajoule up to 4500 GPa. This AIMD isotherm was compared to cold curves based on analytic models implemented in QEOS and QSEM. These have shown that pressures from analytic modeling are lower than pressures from AIMD, and that the pressure-density curvature is changed.

The effect of the presence of oxygen in ICF ablator shells upon the 300-K isotherm was also investigated through the use of two different atomic structures, pointing out differences in pressure reaching up to 10%–15%.

These differences between the cold curves can modify the shock timing that is essential for the quasi-isentropic compression of ICF capsules. Since cold and thermal pressures are additive along the Hugoniot, one can state in a first approximation that a pressure shift on the cold curve at a given density will affect the principal Hugoniot by the same pressure shift, provided the thermal components are equally calculated (e.g., by using a Mie-Grüneisen EOS). Using this hypothesis, we can estimate the differences in shock timing resulting from the choice of cold curve. For example, the conditions of the first shock in an ICF capsule are given by ablation pressure and are roughly 250 GPa and 3 g/cm<sup>3</sup>. AIMD simulations of amorphous CH and amorphous CHO show that the presence of oxygen in the ablator material shifts

the cold curve downward about 30 GPa at 3 g/cm<sup>3</sup> density. This translates into differences in shock velocities of about 1 km/s in order to match the 250 GPa shock pressure on the principal Hugoniot. If we consider that the first shock propagates in  $\approx 100 \mu\text{m}$  in the ablator layer before transmission to the cryogenic D-T, we obtain differences in shock timing  $\approx 250$  ps, which is far beyond the  $\pm 50$  ps shock timing tolerance requirement of the point design capsule specifications.

#### ACKNOWLEDGMENT

We thank M. Torrent and F. Bottin for their help on parallel calculations with ABINIT, and C. Chicanne and S. Le Tacon for material analysis information.

- 
- [1] J. D. Lindl, P. Amendt, R. L. Berger, S. G. Glendinning, S. H. Glenzer, S. W. Haan, R. L. Kauffman, O. L. Landen, and L. J. Suter, *Phys. Plasmas* **11**, 339 (2004).
- [2] S. W. Haan, M. C. Herrmann, P. A. Amendt, D. A. Callahan, T. R. Dittrich, M. J. Edwards, O. S. Jones, M. M. Marinak, D. H. Munro, S. M. Pollaine *et al.*, *Fusion Sci. Technol.* **49**, 553 (2006).
- [3] M. A. Barrios, T. R. Boehly, D. G. Hicks, D. E. Fratanduono, J. H. Eggert, G. W. Collins, and D. D. Meyerhofer, *J. Appl. Phys.* **111**, 093515 (2012).
- [4] G. Huser, N. Ozaki, T. Sano, Y. Sakawa, K. Miyanishi, G. Salin, Y. Asaumi, M. Kita, Y. Kondo, K. Nakatsuka *et al.*, *Phys. Plasmas* **20**, 122703 (2013).
- [5] F. Lambert and V. Recoules, *Phys. Rev. E* **86**, 026405 (2012).
- [6] D. V. Knyazev and P. R. Levashov, *Phys. Plasmas* **22**, 053303 (2015).
- [7] C. Wang, X.-T. He, and P. Zhang, *Phys. Plasmas* **18**, 082707 (2011).
- [8] S. X. Hu, T. R. Boehly, and L. A. Collins, *Phys. Rev. E* **89**, 063104 (2014).
- [9] S. Hamel, L. X. Benedict, P. M. Celliers, M. A. Barrios, T. R. Boehly, G. W. Collins, T. Döppner, J. H. Eggert, D. R. Farley, D. G. Hicks *et al.*, *Phys. Rev. B* **86**, 094113 (2012).
- [10] J.-F. Danel and L. Kazandjian, *Phys. Rev. E* **91**, 013103 (2015).
- [11] D. S. Clark, S. W. Haan, B. A. Hammel, J. D. Salmonson, D. A. Callahan, and R. P. J. Town, *Phys. Plasmas* **17**, 052703 (2010).
- [12] T. R. Boehly, V. N. Goncharov, W. Seka, S. X. Hu, J. A. Marozas, D. D. Meyerhofer, P. M. Celliers, D. G. Hicks, M. A. Barrios, D. Fratanduono *et al.*, *Phys. Plasmas* **18**, 092706 (2011).
- [13] O. L. Landen, J. Edwards, S. W. Haan, H. F. Robey, J. Milovich, B. K. Spears, S. V. Weber, D. S. Clark, J. D. Lindl, B. J. MacGowan *et al.*, *Phys. Plasmas* **18**, 051002 (2011).
- [14] R. M. More, K. H. Warren, D. A. Young, and G. B. Zimmerman, *Phys. Fluids* **31**, 3059 (1988).
- [15] B. I. Bennett, J. D. Johnson, G. I. Kerley, and G. T. Rood, Report LA-7130, Los Alamos National Laboratory (Los Alamos, NM, 1978).
- [16] M. C. Payne, M. P. Teter, D. C. Allan, T. A. Arias, and J. D. Joannopoulos, *Rev. Mod. Phys.* **64**, 1045 (1992).
- [17] H. Huang, D. M. Haas, Y. T. Lee, J. J. Wu, K. A. Moreno, R. B. Stephens, A. Nikroo, M. Stadermann, and S. D. Bhandarkar, *Fusion Sci. Technol.* **63**, 142 (2013).
- [18] S. W. Haan, H. Huang, M. A. Johnson, M. Stadermann, S. Baxamusa, S. Bhandarkar, D. S. Clark, V. Smalyuk, and H. F. Robey, *Phys. Plasmas* **22**, 032708 (2015).
- [19] G. Legay, J. Bray, E. Peche, C. Chicanne, J. Andre, B. Bergeron, and C. Vasselin (private communication).
- [20] T. Plisson (private communication).
- [21] C. Chicanne (private communication).
- [22] Brillouin oscillation is a experimental method to measure an acoustic velocity in a transparent material. A pump beam generates an acoustic wave onto which a probe beam reflects. This creates interferences whose period is related to sound velocity.
- [23] The ABINIT code is a common project of the Catholic University of Louvain (Belgian), Corning Incorporated, and other collaborators.
- [24] X. Gonze, J.-M. Beuken, R. Caracas, F. Detraux, M. Fuchs, G.-M. Rignanese, L. Sindic, M. Verstraete, G. Zerah, F. Jollet *et al.*, *Comput. Mater. Sci.* **25**, 478 (2002).
- [25] F. Bottin, S. Leroux, A. Knyazev, and G. Zerah, *Comput. Mater. Sci.* **42**, 329 (2008).
- [26] P. E. Blöchl, *Phys. Rev. B* **50**, 17953 (1994).
- [27] M. Torrent, F. Jollet, F. Bottin, G. Zerah, and X. Gonze, *Comput. Mater. Sci.* **42**, 337 (2008).
- [28] W. Kohn and L. Sham, *Phys. Rev.* **140**, A1133 (1965).
- [29] J. P. Perdew, K. Burke, and M. Ernzerhof, *Phys. Rev. Lett.* **77**, 3865 (1996).
- [30] P. Minary, G. J. Martyna, and M. E. Tuckerman, *J. Chem. Phys.* **118**, 2510 (2003).
- [31] F. Zhang, *J. Chem. Phys.* **106**, 6102 (1997).
- [32] D. R. Lide, *CRC Handbook of Chemistry and Physics*, 90th ed. (CRC, Boca Raton, FL, 2009).
- [33] J.-P. Poirier, *Introduction to the Physics of the Earth's Interior*, 2nd ed. (Cambridge University Press, Cambridge, U.K., 2009).
- [34] F. Birch, *Phys. Rev.* **71**, 809 (1947).
- [35] P. Vinet, J. Ferrante, J. R. Smith, and J. H. Rose, *J. Phys. C: Solid State Phys.* **19**, L467 (1986).
- [36] W. B. Holzapfel, *High Press. Res.* **16**, 81 (1998).
- [37] G. Salin (private communication).
- [38] J. F. Barnes, *Phys. Rev.* **153**, 269 (1967).
- [39] D. A. Liberman, *Phys. Rev. B* **20**, 4981 (1979).
- [40] R. Piron and T. Blenski, *Phys. Rev. E* **83**, 026403 (2011).